

Journal of Materials Chemistry A

Accepted Manuscript



This is an *Accepted Manuscript*, which has been through the Royal Society of Chemistry peer review process and has been accepted for publication.

Accepted Manuscripts are published online shortly after acceptance, before technical editing, formatting and proof reading. Using this free service, authors can make their results available to the community, in citable form, before we publish the edited article. We will replace this *Accepted Manuscript* with the edited and formatted *Advance Article* as soon as it is available.

You can find more information about *Accepted Manuscripts* in the [Information for Authors](#).

Please note that technical editing may introduce minor changes to the text and/or graphics, which may alter content. The journal's standard [Terms & Conditions](#) and the [Ethical guidelines](#) still apply. In no event shall the Royal Society of Chemistry be held responsible for any errors or omissions in this *Accepted Manuscript* or any consequences arising from the use of any information it contains.



Journal Name

ARTICLE

Novel dual-petals nanostructured WS₂@MoS₂ with enhanced photocatalytic performance and a comprehensive first-principles investigation

Received 00th January 20xx,
Accepted 00th January 20xx

DOI: 10.1039/x0xx00000x

www.rsc.org/

Honglin Li, Ke Yu*, Chao Li, Bangjun Guo, Xiang Lei, Hao Fu and Ziqiang Zhu

For the first time, the novel dual-petals nanostructured WS₂@MoS₂ heterojunction was fabricated via a facile two-step approach and explored as photocatalyst for the photodegradation of methylene blue (MB). In the light of the results obtained from experiments, a reasonable formation mechanism for the nanopetals (NPs) structured WS₂ was proposed, in which the pretreatment of ball milling had played an important role for the formation of WS₂ NPs that subsequently acted as the base material to grow curly MoS₂ sub-NPs. Because the dual-petals nanostructured WS₂@MoS₂ possessed plenty of active sites that originated from its unique structural characteristic with densely stacked MoS₂ nanopetals and an effective separation of photoinduced carriers, it exhibited significantly enhanced photocatalytic activity and obviously exceeded the pristine MoS₂/WS₂. In order to propose a scientific explanation of the corresponding enhancement mechanism, we further conducted the comprehensive first-principles calculations to investigate the corresponding structural, electrical, and optical properties of this WS₂@MoS₂ composite. The results revealed that the calculated band gap of the WS₂@MoS₂ composite was narrower than that of pristine WS₂ and MoS₂, meanwhile, it had a well-defined stagger type-II band alignment, leading to the photoexcited electrons injected into the conduction band minimum (CBM) of MoS₂ from the CBM of WS₂. This separation of carriers can restrain the photogenerated e⁻-h⁺ pairs' recombination and prolong the lifetime of carriers for the proper interface charge distribution. In short, the calculated results fully explained the reason why the composite presented an improved photocatalysis and provided valuable references for the future studies.

1 Introduction

With the rapid development of modern science and technology, the applications of solar energy conversion and the related pollution treatment by various semiconductor-based photocatalysis materials have attracted considerable attentions over the past few years.^{1, 2} In order to maximize the efficiency for solar energy utilization, the purposive design and fabrication of an efficient semiconductor-based photocatalyst through a certain form of modification has become a worldwide pursuit and is the key to the photocatalysis.^{3, 4} Because of the correlation between chemical properties and structural characteristics, the targeted design and synthesis of semiconductor materials with diverse micro-/nano-structure provide many more possibilities to perfect the overall performance of photocatalysts.⁵⁻⁷ Therefore, researchers have been committed to fabricating semiconductor based materials with a variety of architectural structural morphologies to achieve special or enhanced performances for diverse photocatalytic applications.

Ever since the discoveries and applications of graphene-like nanomaterials, two-dimensional (2D) layered transition metal dichalcogenides have been a hot area for several years in industrial and scientific fields for their special properties, such as narrow band gap, diverse structures and morphologies.⁸ Of particular note is that the 2D-layered structures with high specific surface area can provide massive active sites for various reactions and these nanosized structures can also act as the matrix to fabricate different types of composites with a large interfacial contact, which is especially useful for the catalysis related applications.⁹ Among various 2D-layered materials, WS₂/MoS₂, composed of W/Mo atoms sandwiched between two hexagonal S atom layers, have displayed many outstanding performances and can be widely applied in many fields such as secondary lithium batteries, transistors, solid superlubricants, hydrodesulfurization of crude oil and catalysts.¹⁰⁻¹³ For example, Zhou *et al.*¹⁴ have successfully fabricated TiO₂ nanobelts coated by few-layers MoS₂ via a hydrothermal reaction, which exhibited improved photocatalysis ability in hydrogen evolution and rhodamine B (RhB) degradation. Jana *et al.*¹⁵ have fabricated WS₂ thin films through electrodeposition on ITO coated glass substrate using sodium tungstate and thioacetamide as W and S sources. It was found that the mixed phase of WS₂/WO₃ showed a better catalytic activity for the photodegradation of phenol. These pioneering researches have clearly demonstrated that 2D-

Key Laboratory of Polar Materials and Devices (Ministry of Education of China),
Department of Electronic Engineering, East China Normal University, Shanghai
200241, China

*Corresponding author. E-mail address: yk5188@263.net

layered materials have huge potential in the field of photocatalysis.

The preparation of transition-metal chalcogenides based 2D structured materials have sparked plenty of new discoveries in condensed-matter physics and electronics.¹⁶ Many different synthesis methods have been explored to fabricate the WS₂/MoS₂ based materials with a diversity of morphologies and structures until now (nanoparticles, nanowires, nanotubes, nanorods, nanoflowers, etc.). The preparation approaches involve high-temperature sulfurization,¹⁷ thermal decomposition,¹⁸ magnetron sputtering,¹⁹ chemical vapor deposition,²⁰ laser ablation²¹ as well as the most commonly used hydrothermal route.²² Generally, the miniaturization of these 2D structured materials can modulate the electrons transport and enhance the corresponding performance which mainly derive from the enlarged surface area. Seo *et al.* prepared 2D WS₂ NSs with the aid of surfactant by processing 1D tungsten oxide nanorods.²³ Li *et al.* fabricated WS₂ nanoflakes by using tungsten oxide nanorods as precursors.²⁴ Zhou *et al.* developed a facial hydrothermal method to fabricate porous MoS₂ without using any sacrificial template, the products exhibited significantly enhanced catalysis activity for the increased active edge sites.²⁵ Anyhow, it still remains a great challenge to fabricate these 2D structured WS₂/MoS₂ through a reproducible and scalable approach.

Although considerable researches have been conducted for the WS₂/MoS₂ based structures, there is still no report regarding to the WS₂@MoS₂ based composite material employed as co-catalysts for the photodegradation usage. In this paper, the novel dual-petals nanostructured WS₂@MoS₂ has been fabricated for the first time through a simple and reproducible two-step approach, including the ball milling combined with an annealing process using WO₃ and S as the starting materials and a following hydrothermal route. The as-prepared dual-petals nanostructured WS₂@MoS₂ demonstrated a well defined hierarchy architecture with separated WS₂ sheets and thin MoS₂ sub-petals.¹⁶ To our knowledge, this is the first report on the synthesis of WS₂@MoS₂ composite through this two-step approach. On the basis of its unique structure and morphology, the possible reaction processes and formation mechanisms for WS₂/MoS₂ have been detailedly explored. Because of its novel nanostructure characteristics with dispersed WS₂ petals and closely attached MoS₂, the composite could provide massive rims and edges to participate in the corresponding photocatalytic reactions, also, the well-defined stagger arrangement of energy bands would further facilitate the separation of photoinduced charges and prolong the lifetime of carriers. In order to illuminate the corresponding properties from a theoretically sound perspective, we further performed the first principles calculation to investigate the interaction between WS₂/MoS₂ and tried to clarify the underlying enhancement mechanisms. In brief, all theoretical calculations conducted in this work have created a deep understanding of the experimental results and also can be extended for future studies of the other layered heterojunctions.

2 Experimental

2.1 Synthesis of dual-petals nanostructured WS₂@MoS₂

Firstly, in a typical synthesis of WS₂ NPs, 3 g WO₃ and 10 g S were mixed together and put in an argon filled planetary ball mill operated at 400 rpm for 24 h with stainless balls as milling media. Then, 5 g sulfur and 1 g ball-milled mixture were pushed into the tube furnace successively that had been preheated to 600 °C under pure argon. The temperature was kept for 2 h and then naturally cooled down to room temperature. Finally, the black WS₂ powder was obtained. As for the synthesis of pristine MoS₂ nanoflower, 1.2 g Sodium molybdate dihydrate and 1.6 g thioacetamide were served as Mo and S source, respectively. The above solutes together with 0.6 g oxalic acid were dissolved in 80 ml deionized water to adjust the pH value to an acid environment. The mixed liquor was magnetic stirred for about 30 min and then transferred to a 100 ml Teflon lined stainless-steel autoclave.²⁶ Finally, the autoclave was sealed and heated at a drying oven in 180 °C for 24 h. After cooled down to room temperature naturally, the black resultants were generated and attached on the inner wall of liner. These black products were cleaned by an ultrasonic cleaning with ethanol and distilled water alternately for several times to remove impurities, then dried in a vacuum at 50 °C for 12 h to obtain black MoS₂ powders.

As for the fabrication of dual-petals nanostructured WS₂@MoS₂, 0.1 g WS₂ NPs was dispersed in 80 mL deionized water. 0.6 g Sodium molybdate dehydrate, 0.8 g thioacetamide and 0.3 g oxalic acid were then added to the above mixed solution. The following procedures were the same with the synthesis of the pristine MoS₂.

2.2 Sample characterization

A field emission scanning electron microscopy (FESEM, JEOL-JSM-6700F, operating accelerating voltage of 20 kV) was used to analyze the morphology and structure of the synthesized nanostructures, XRD measurements were conducted using Cu K α radiation ($\lambda = 1.5418 \text{ \AA}$) (Bruker D8 Advance diffract meter) and transmission electron microscopy (TEM, JEOL-JEM-2100) at the accelerating voltage of 200 kV. X-ray photoelectron spectrometry (XPS) measurements were conducted with an ESCALAB 250Xi instrument using monochromatic Al K α radiation. All the above measurements were performed at room temperature.²⁷

2.3 Photocatalytic measurements

In this part, the photocatalysis capacities of different samples were evaluated by the photodegradation of MB at room temperature under light irradiation. The highest optical absorption of MB at 664 nm was used as monitor wavelength of photodegradation. Firstly, 0.1 g as-prepared samples were added to 100 mL MB aqueous solution (40 mgL⁻¹). In order to establish the adsorption/desorption equilibrium, the mixed liquor was stirred for 1 h in dark before photodegradation reaction. The reactor was situated in a glass container and cooled by flowing water to eliminate the possible thermal influence. The visible-light source was a 500 W Xe lamp with cutoff filter ($\geq 400 \text{ nm}$), which was placed 5 cm away from the

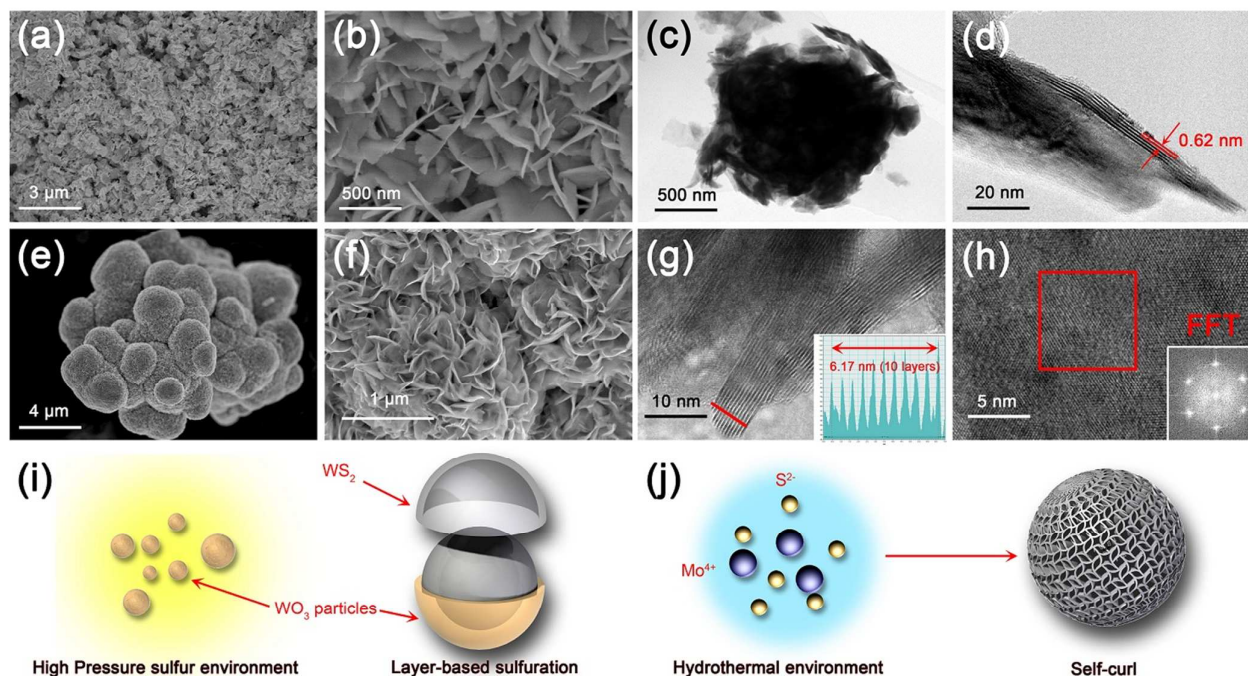


Fig. 1 (a-b) SEM images of the pristine WS_2 NPs under different magnifications, (c) and (d) are TEM and HRTEM of the pristine WS_2 NPS, respectively. (e-f) SEM images of the pristine MoS_2 nanoflower. (g) HRTEM image of a MoS_2 petal. (h) FFT pattern of the red box. (i-j) Schematic diagram for the formation processes of WS_2 NPs and MoS_2 nanoflowers, respectively.

liquid surface of the MB suspension. The absorption surveys were conducted by a UNICO 2802 spectrophotometer at an interval of 20 minutes for 120 min. The mineralization degree of the corresponding solutions was analyzed by a total organic carbon (TOC) analyzer (AnalytikJena, Multi N/C 2100S). Photocurrent measurement was performed by an electrochemical analyzer (CHI 660D, China) in a three-electrode system. A Pt wire (purity 99.99%) and Ag/AgCl (saturated KCl) acted as the counter electrode and the reference electrode, respectively, 0.1 M Na_2SO_4 solution used as the electrolyte.

2.4 Computational details

In this work, we performed a comprehensive first-principles calculations to study the detailed properties of this heterogeneous structure to give the theoretical basis of the promoted photocatalytic activity. All calculations were performed using DFT, as implemented in the Vienna ab initio Simulation Package (VASP).²⁸ The valence electrons considered were: Mo (4p5s4d), W (6s5d) and S (s2p4), respectively. The generalized gradient approximation (GGA) functional of Perdew, Burke and Ernzerhof (PBE) was used to deal with the exchange and correlation potentials.²⁹ The spacing of 15 Å was used to avoid interlayer interactions. A $5 \times 5 \times 1$ Monkhorst-Pack k-point sampling for the Brillouin zone k-point mesh and a 450 eV cutoff energy were used for the calculations. Since the absence of strong bonding interactions for the layer structured WS_2 and MoS_2 , weak van der Waals (vdW) interactions are expected to play a leading role, thus the GGA of PBE form with vdW correction proposed by Grimme is chosen to optimize

their geometric structures for its reasonable description of the corresponding vdW interactions.³⁰ All initiating structures have been fully relaxed until the convergence criteria of energy and force were less than 10^{-5} eV and 0.01 eV Å⁻¹, respectively.

To further investigate the optical properties of the different structures, the optical absorption spectra are calculated by substituting into complex dielectric function

according to the equation: $\alpha_{\text{ads}} = \sqrt{2} \omega (\sqrt{\varepsilon_1^2(\omega) + \varepsilon_2^2(\omega)} - \varepsilon_1(\omega))^{1/2}$, where $\varepsilon_1(\omega)$ and $\varepsilon_2(\omega)$ are the real and imaginary parts, respectively. $\varepsilon_1(\omega)$ and $\varepsilon_2(\omega)$ are the averaged values on the three polarization vectors when take the tensor nature of the dielectric function into consideration.

3 Results and discussion

Nanopetals structured WS_2 materials have been synthesized by ball-milling the original materials WO_3/S and the following heat treatment at 600 °C as mentioned above. Different magnifications SEM images of the WS_2 NPs are presented in Fig. 1a and b. As revealed in the Fig. 1b, all NPs are well separated and obviously differ from the previously reported WS_2 nanoplates with close stacked architecture.²⁵ Individual WS_2 NP is generally hundreds of nanometer in length and dozens of nanometers in thickness. It is observed that most of WS_2 NPs are overlapped loosely and the petals are grown in a straight way. A further study of the morphology and microstructure for the fabricated WS_2 NPs can be obtained

from their TEM and HRTEM surveys shown in Fig. 1c and d. The WS₂ layers are naturally unstable and tend to stack through the weak vdW force. The HRTEM image shown in Fig. 1(d) indicates that the WS₂ NPs are all crystallized with a well defined lattice fringes of 0.62 nm, and in particular, the well-defined contour.

To better understand the formation mechanism of WS₂ NPs, we propose a growth process as shown in Fig. 1i to systematically elucidate the formation mechanism of this 2D NPs. The synthesized WS₂ NPs are all hexagonal structured nanopetals as analyzed above for the intrinsic symmetry of corresponding lattices, which can be ascribed to the layer-by-layer formed WS₂ shell during high-temperature annealing process. It is reasonable that WO₃ particles can be uniformly covered by sulfur under high pressure sulfur environment and form a stable shell after ball milling for 24 h. Then a further sulphurize the inner oxide core to produce WS₂ NPs is followed by a rapid stripping process according to the “outside-in” mechanism after a high-temperature annealing which was proposed by Feldman *et al.*³¹ The outer spheres are instability and tend to break into pieces in the shape of NPs and finally form nanopetals structured WS₂. In brief, WS₂ NPs are produced by a progressive exfoliation of the outer sulfide layers toward the inner WO₃ spheres. It is concluded that the ball milling pretreatment plays a critical role in the final formation of WS₂ NPs. This approach can certainly activate WO₃, since the wide distribution of sulfur will facilitate the rapid and efficient sulfurization process. Besides, the redundant S can also prevent WS₂ from reacting with the trace O₂, this can be confirmed by the following XRD measurements.

Generally, the WS₂ nanostructures should be prepared in a reducing atmosphere (H₂S/H₂) by the sulfurization of WO₃.³¹ This process contains a reduction and the following sulfurization steps. Yang *et al.*³² synthesized inorganic fullerene-like WS₂ by using S and WO₃ as reactants in H₂ atmosphere. In the related reaction processes, WO₃ particles were firstly reduced into suboxide WO_x under reducing gas atmosphere, and then sulfurized to the final WS₂, in which many intermediate suboxides, such as WO_{3-x}, W₁₈O₄₉ and W₂₀O₅₈, could be detected. There is no other suboxides detected in the present products as analyzed by the following XRD survey, indicating the high purity of the fabricated WS₂. The overall reaction can be expressed as: 2WO₃ + 7S = 2WS₂ + 3SO₂. This reaction relies on the activation effect of ball milling, which is considered to be able to break WO₃ particles into small parts for sulfur wrapping more closely and accelerate the reaction to reach a favorable sulfurization. Generally, the sulfurization happens only after the reduction of WO₃ nanoparticles when H₂ is involved at high temperatures as Yang *et al.*³² reported. This indirect process would slow the rate of sulfurization since the break of strong oxygen-metal bond requires a high energy.³¹ In this work, the role of H₂ in the previous reports can be substituted by S in the process of ball milling and the sulfurization of WO₃ becomes much more easier. Consequently, the present sulfurization is more effective and faster after being activated by ball milling

pretreatment than the reaction with H₂ involvement at high temperatures.³¹ In brief, a possible reaction process for the fabrication of WS₂ NPs is proposed based on the above surveys and discussions. A close integration of S and WO₃ can be achieved through ball-milling pretreatment which acts as a mechanical activation role and the WO₃ particles are tightly covered by excess S. After the annealing, WS₂ NPs generated and peeled off from WO₃ particles. A schematic diagram for the formation processes of WS₂ NPs is presented in Fig. 1i.

The morphology and microscopic structures of the pristine MoS₂ are also characterized by SEM and TEM images, the corresponding figures are shown in Fig. 1e-h. As exhibited in Fig. 1e, each MoS₂ sphere reveals an average diameter of 2 to 3 μm. The surface of the MoS₂ shows a flowerlike morphology and mainly consisted by 2D nanopetals and the synthesized nanopetals grow in a high density, which are freely and tightly aggregated together as displayed in Fig. 1f. It can be seen that the 2D structured petals intersected together disorderly and pointed to the center of sphere to form the spherical shape as shown in the Fig. 1f. In the Fig. 1g and h, TEM and HRTEM measurements are performed to further characterize the morphology and construction of MoS₂ nanoflowers. The HRTEM image of Fig. 1g shows a single MoS₂ petal, which further proves the 2D aggregated nature of pristine MoS₂ and the synthesized pristine MoS₂ spherical structure grows in a high density way and tends to stack with a 0.62 nm interlayer distance. The lattice-resolved HRTEM image shown in Fig. 1h and the corresponding FFT pattern indicates the highly crystalline characteristic and undoubtedly attributes to the hexagonal MoS₂.

As for the formation of pristine MoS₂ nanoflowers, it associates with the nucleation under 180 °C in hydrothermal environment of amorphous primary nanoparticles. Numerous amorphous MoS₂ structures take shape in the solution during the primary reaction period as shown in Fig. 1j, in which the added NH₂CNSNH₂ acts as S resource and reductant jointly. These primary structures can spontaneously and freely aggregate into spheres and then curl to structured petals gradually in the surface for the layered nature of MoS₂ when the temperature and pressure exceeds 180 °C and 1 MPa, respectively.

Fig. 2 shows a sequence of SEM and TEM images of the dual-petals nanostructured WS₂@MoS₂ composite. The morphology and microscopic structure of the synthesized composite are characterized by SEM shown in Fig. 2a. In general, it is markedly different from the pristine WS₂ and MoS₂ shown in Fig. 1. It can be seen that each WS₂@MoS₂ composite NS shows an average length of about 0.5 μm. Fig. 2a demonstrates the overall morphology of WS₂@MoS₂ composite nanopetals, which possess massive smaller sub-petals and are widely and tightly attached to the even surface of WS₂ NS in the form of curls. These sub-petals are preliminarily considered belong to the MoS₂ nanopetals as shown in the insert Fig. 2a. A further investigation of this WS₂@MoS₂ dual-petals nanostructured composite should be conducted based on TEM and HRTEM surveys to characterize

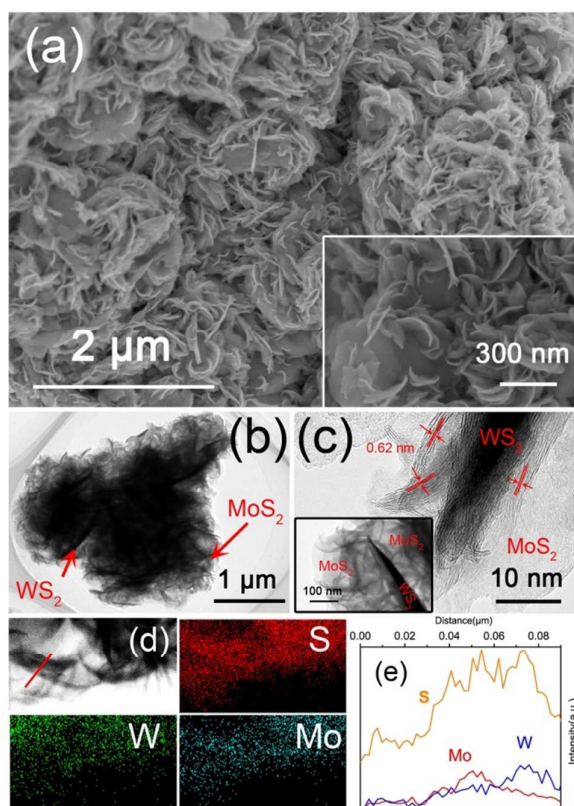


Fig. 2 (a) SEM images with different magnifications of the fabricated dual-petals nanostructured $WS_2@MoS_2$. (b) The overall medium-magnification TEM image of the $WS_2@MoS_2$. (c) High resolution TEM of a $WS_2@MoS_2$ petal with the details of the binding site. Insert figure shows the low-magnification TEM of a single $WS_2@MoS_2$ petal. (d) The EDX mapping images of S, W and Mo. The red line denotes the line scan range of the elements distribution. (e) The elements intensity signals along the red line as shown in Fig. 2d.

their hierarchical structures. Fig. 2b shows the low magnification TEM image of $WS_2@MoS_2$. Clearly, it is markedly different from the pristine WS_2 shown in Fig. 1c. The edge sections are wrapped by a circle of semitransparent substance which belongs to the MoS_2 sub-petals. The HRTEM image of Fig. 2c provides a further perfect illustration of the coexistence of WS_2 and MoS_2 . The thick and straight parts attribute to the WS_2 petals while the curly and semitransparent parts belong to the MoS_2 petals. The fringes of $d=0.62$ nm shown in Fig. 2c is in agreement with the (002) plane and also indicates that the fabricated MoS_2 petals grow in a crystallization way. The insert Fig. 2c under medium-magnification exhibits a more clear coexistence evidence of $WS_2@MoS_2$, which differ from the well-defined pristine WS_2 petal shown in Fig 1d. From the elemental mapping of Fig. 2d for the composite, it can be seen that the extensive distribution of S, W and Mo. Moreover, the line scan of the region marked in red line in Fig. 2d is presented in Fig. 2e, it clearly exhibits the different distribution of W and Mo, in which the dense and straight part reveals a stronger W single. In brief, the above SEM and TEM investigations of dual-petals nanostructured $WS_2@MoS_2$ hetero-structure convincingly demonstrate the formation of the corresponding 3D

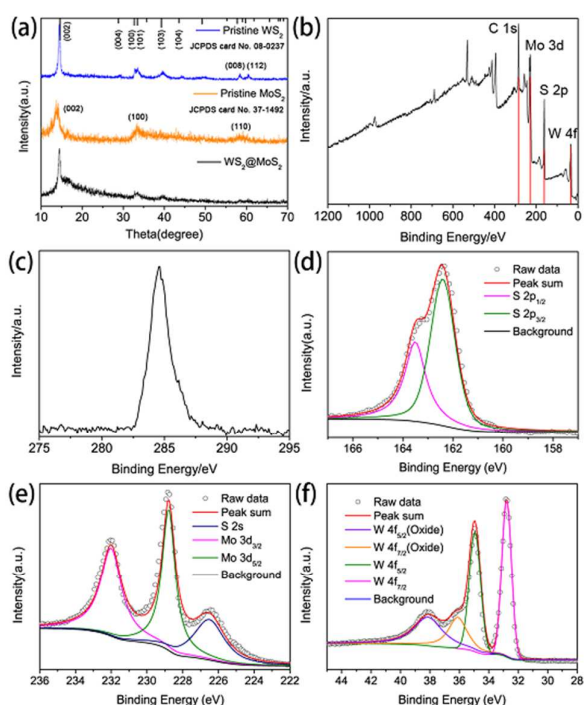


Fig. 3 (a) XRD patterns of the pristine WS_2/MoS_2 and $WS_2@MoS_2$ composite, (b) Typical overall XPS pattern, (c) C 1s spectrum, (d) S 2p spectrum, (e) Mo 3d and S 2s spectra, (f) W 4f spectrum for $WS_2@MoS_2$ composite. Experimental data points are fitted by Voigt (mixed Lorentzian–Gaussian) line shapes after the application of a Shirley background.

hierarchical architecture. MoS_2 sub-nanopetals are clearly showed from Fig. 2a to c and it is apparent that they are widely and uniformly grown on WS_2 petals. As for the formation mechanism of $WS_2@MoS_2$, we consider the formation of MoS_2 sub-nanopetals are greatly affected by the existence of WS_2 in hydrothermal environment. In the process of the hydrothermal reduction from sodium molybdate dihydrate to MoS_2 , it may grow on these highly crystallized WS_2 petals that act as matrix to form MoS_2 sub-nanopetals. The MoS_2 itself is 2D structured and has the nature of growing in a form of curls in this environment, it will result in the confined growth of dual-petals nanostructured $WS_2@MoS_2$ eventually. In the absence of WS_2 , the pristine 2D MoS_2 petals prefer to roll up to form closed structures with flowers on the face in order to decrease the number of dangling bonds and the total energy of the system, which is significantly different from this $WS_2@MoS_2$ composited structure.

A typical XRD pattern for the synthesized WS_2 NPs is shown in Fig. 3a, which presents a high purity of WS_2 for the as-prepared sample. All the reflections can be assigned to the hexagonal WS_2 (JCPDS#08-0237). The distance between two lattice planes along (002) is 0.621 nm. This value is slightly larger than that of 0.618 nm for the standard 2H- WS_2 , indicating the presence of strain in the layers. The purity and crystalline phase of the hydrothermally synthesized pristine MoS_2 are also characterized by XRD patterns. The yellow curve of the pattern shows XRD spectrum of the as-prepared MoS_2

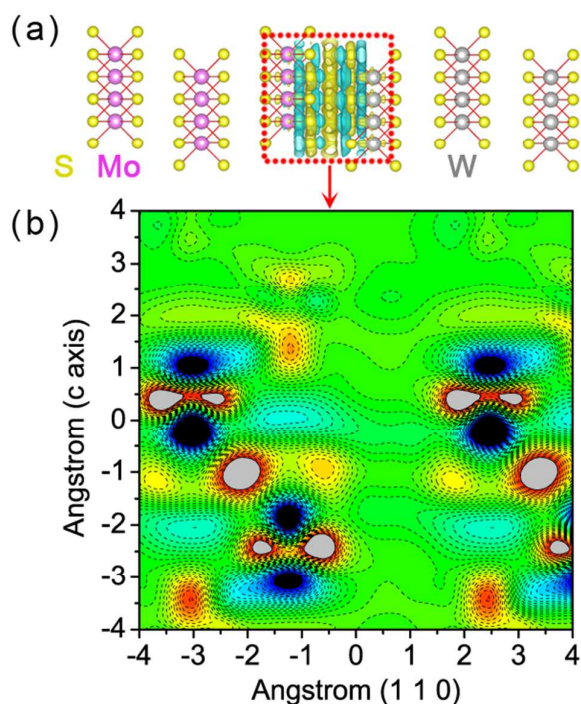


Fig. 4 (a) The 3D different charge density distribution of the WS₂@MoS₂ heterogeneous structure along the (001) direction. The cyan and yellow regions represent the charge depletion and accumulation space, respectively. (b) The corresponding 2-d density plotted in plane across basal plane and parallels c axes. The dashed lines denote the regions of charge accumulation/depletion.

nanoflower, it corresponds well with the standard hexagonal MoS₂ (JCPDS#37-1492) and no other impurity peak is observed. The observed diffraction peaks at $2\theta=14.2^\circ$, 33.2° and 58.8° can be well attributed to the (002), (100) and (110) planes of hexagonal MoS₂, respectively. There is also no other impurity peak found in the spectrum, implying a high purity of the fabricated MoS₂ structure. All the diffraction peaks match well with the hexagonal phase of MoS₂, while the weak diffraction of (002) plane implies the low crystallinity, indicating the petals of MoS₂ constituted by a few layers of MoS₂, which has a significant difference with the ball-milling method pretreated and then annealed WS₂ sample. As for the dual-petals nanostructured WS₂@MoS₂, it clearly shows the coexistence of highly crystallized WS₂ and poorly crystallized MoS₂. A further characterization based on XPS measurement will be conducted and the elements constitution of the WS₂@MoS₂ composite is also investigated.

Fig. 3b-f present the typical overall XPS spectrum and a series of high-resolution XPS spectra of W 4f, Mo 3d, and S 2p. As shown in the overall XPS spectrum, W, Mo, S and C can be detected on the surface. The observed peak of C 1s shown in Fig. 3c is originated from the signal of carbon in the instrument and it is inherent. As presented in Fig. 3d, two peaks can be decomposed from 157 eV to 167 eV.³³ The peaks at 163.5 and 162.4 eV attribute to the coexistence of S 2p_{1/2} and S 2p_{3/2}. Two main peaks of Mo 3d_{3/2} (232.1 eV) and Mo 3d_{5/2} (228.8 eV) are typical characteristics of MoS₂ and the peak at 226.5 eV

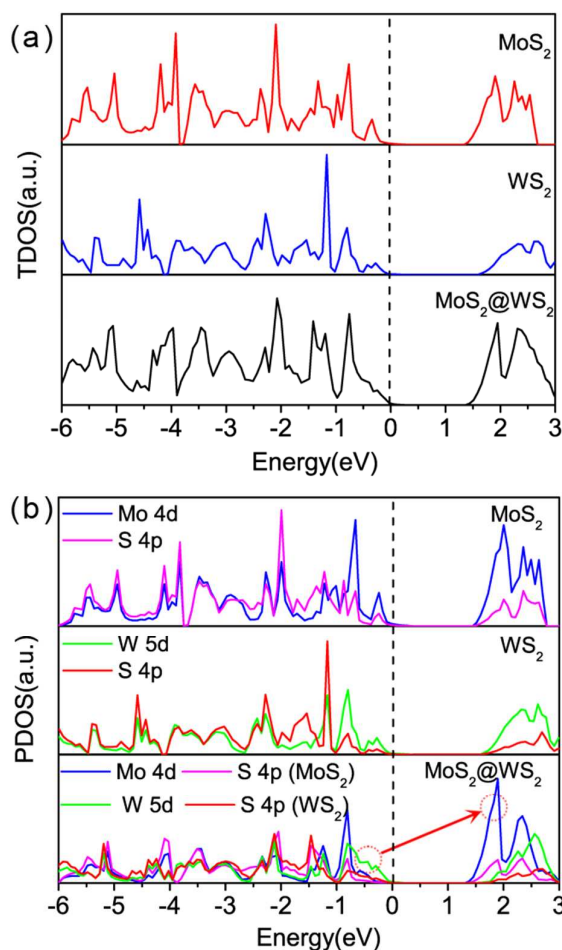


Fig. 5 (a) The total density of states (TDOS) and corresponding (b) partial density of states (PDOS) of pristine WS₂/MoS₂ and WS₂@MoS₂ composite. The Fermi level is represented by the short dashed line.

ascribed to S 2s (Fig. 3e). The W 4f_{7/2} and W 4f_{5/2} peaks for W⁴⁺ in WS₂ are at binding energies of 32.8 and 34.9 eV, and for W⁶⁺ in WO₃ are at 36.0 and 38.1 eV (oxide state).³⁴ In order to further theoretically investigate the interaction between WS₂ and MoS₂ through a visual manner, we performed charge density difference analysis based on the first-principles calculation.

In order to investigate the electron configuration of the WS₂@MoS₂ heterogeneous structure, we calculated the charge density difference of this composite. As shown in Fig. 4a, the 3D charge density difference surface was obtained by subtracting the calculated electronic charges of the individual WS₂ and MoS₂ from that of the WS₂@MoS₂ composite. It should be noted that the computed model in this work is based on the experiment as shown in HRTEM measurement that the growth direction is along (001) plane. The charge density difference is expressed as:

$$\Delta n(\mathbf{r}) = n_{\text{WS}_2@MoS_2}(\mathbf{r}) - n_{\text{WS}_2}(\mathbf{r}) - n_{\text{MoS}_2}(\mathbf{r})$$

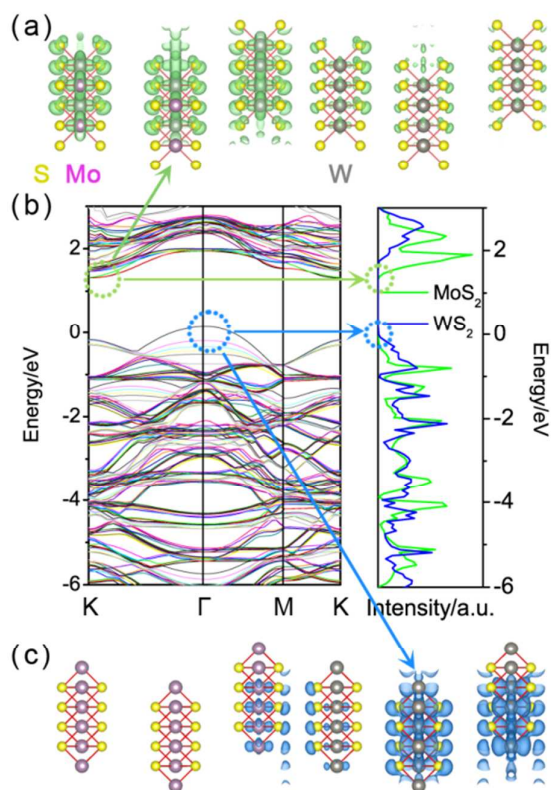


Fig. 6 (a) and (c) The partial charge density of the CBM and the VBM, respectively. (b) The bandstructure and PDOS of WS₂ and MoS₂ in the composite.

where $n_{\text{WS}_2@MoS_2}(\mathbf{r})$ is the electron density of the WS₂@MoS₂ composite, whereas $n_{\text{WS}_2}(\mathbf{r})$ and $n_{\text{MoS}_2}(\mathbf{r})$ are the separate electron density of WS₂ and MoS₂, respectively.³⁵ All atoms were kept at the same positions as they were in the integral structure in computing of $n_{\text{WS}_2}(\mathbf{r})$ and $n_{\text{MoS}_2}(\mathbf{r})$. The cyan and yellow regions represent charge depletion and accumulation, respectively. It is shown that the charge transfer occurs mainly between the contact area and the around S atoms. The closer the S atoms are near the surface, the more charge transfer occurs. Furthermore, the charge transfer region of WS₂ and MoS₂ have a clear distinction as shown in Fig. 4b, the corresponding 2D density plot. The depletion region around S atoms of WS₂ in the interface are significantly larger than that of MoS₂, which will effectively separate the electron-hole pairs under the polarized field.³⁶ A further Bader charge analysis elucidates that there is an average charge transfer of 0.01 e from WS₂ to MoS₂.³⁷ Under the action of e^-h^+ pairs separation, the photoinduced carriers' lifetime can be effectively prolonged, which is beneficial for photocatalysis. In this regard, the WS₂@MoS₂ heterogenous structure can impose a positive effect on the improved photocatalytic performance.

To further investigate the carriers migration between WS₂ and MoS₂, the TDOS and the PDOS from -6 to 3 eV were calculated for the pristine WS₂/MoS₂ and the WS₂@MoS₂ composite as presented in Fig. 5. The highest occupied state

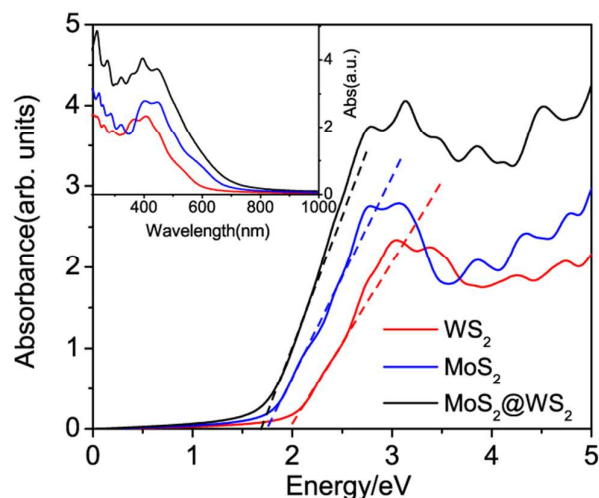


Fig. 7 Absorption spectra of WS₂, MoS₂ and WS₂@MoS₂ composite.

was chosen as the Fermi level and set to zero as the reference.³⁸ From the PDOS of the MoS₂, it can be seen that the valence band maximum (VBM) and CBM of the MoS₂ are predominantly composed of Mo 4d states and have some hybridization with the S 4p states.³⁹ There is an obvious hybridization between the Mo 4d orbitals and the S 4p orbitals around the CBM, leading to a large splitting between the bonding and anti-bonding states. The VBM and CBM of the WS₂ surface is mainly composed of W 5d states, including some hybridization with S 4p states. The electronic structure of the WS₂@MoS₂ composite structure can be effectively modified by compounding the two separated structures. The calculated band gap of the WS₂@MoS₂ composite is obviously smaller than the two separated portions. The VBM and CBM of the MoS₂ in the WS₂@MoS₂ composite move to a lower energy region compared with that of the pristine MoS₂, which will lead to a shift in the optical absorption edge of the WS₂@MoS₂ composite towards the long wavelength direction. Under visible-light irradiation, it is possible that the electrons in the W 5d states prefer to be excited to the Mo 4d and S 4p states, resulting in an easier electronic transition from the VB to the CB in the hybrid WS₂@MoS₂ structure than that in pristine WS₂ and MoS₂. Therefore, the combination of the WS₂ and MoS₂ is expected to improve the photocatalytic activity by enhancing its visible-light response.

To further explore the distribution of the charges, the partial charge density of the CBM/VBM for WS₂@MoS₂ composite are calculated and show in Fig. 6. The results reveal that the electronic densities of CBM for the composite is mainly composed of Mo 4d and a portion of S 4p orbitals, while the VBM are nearly localized around the W 5d orbital. When visible light irradiates the WS₂@MoS₂ composite, the W 5d electrons in the VBM are excited to the Mo 4d and S 4p orbitals, which is also in agreement with the above DOS analysis shown in Fig. 5b, implying the photogenerated e^-h^+ pairs can be well separated by the interface charge transfer,

resulting in the enhanced photocatalytic activity for the WS₂@MoS₂ composite.⁴⁰ The above model and calculations also accord well with Zhang *et al.* reported results.⁴¹

Besides, we also calculated the work functions of WS₂ and MoS₂ by aligning the Fermi level relative to the vacuum energy level. The work functions for WS₂ and MoS₂ are calculated to be 4.63 and 4.87 eV, respectively. Because the work function position of WS₂ is higher than that of MoS₂, the electrons will flow from WS₂ to MoS₂ if they contact. Therefore, MoS₂ will be negatively charged near the interface while WS₂ will be positively charged for the involvement of electrostatic and the corresponding electrons rich environment will take sharp for the MoS₂. Afterwards, a built-in electric field directed from WS₂ to the MoS₂ will be established when two portions acquire an equalized Fermi level, which can halt the charge diffusion between WS₂ and MoS₂. Under visible light irradiation, both WS₂ and MoS₂ will absorb photons and excite the electrons in the VB to the CB and leave holes in the VB. For the formation of stagger band gap arrangement at the interface, the photogenerated electrons of WS₂ will be injected into the CB of MoS₂, while the photogenerated holes can be largely gathered in the VB of MoS₂. Therefore, the recombination of e⁻-h⁺ is effectively restrained. Besides, the presence of the built-in electric field can further strengthen the separation of photogenerated e⁻-h⁺ pairs. It is thus concluded that the photocatalytic activities of WS₂@MoS₂ composite can be significantly improved as analyzed above.

To investigate how the visible-light absorption changes for the WS₂@MoS₂ composite, the wavelength/energy dependent absorption coefficient is calculated and demonstrated in Fig. 7. For comparison, the absorption coefficients of the pristine WS₂ and MoS₂ are also included. For the three structures, the main peaks exist around 400 nm. The absorption edge for pristine WS₂ and MoS₂ are calculated at approximately 2.0 and 1.7 eV (620 and 729 nm), respectively, which are significantly larger than the band gap of the two pristine structures. A similar phenomena have also been observed by Wu *et al.*⁴² and Wang *et al.*³⁶ They considered that the orbital overlap and the optical transitions between CBM and VBM are negligible, resulting in the light absorption in a high energy region. It is shown that the WS₂@MoS₂ composite displays improved absorption. In comparison with the two separated pristine structures, the composite exhibits much more effective UV absorption and improved response in low-energy region. Generally speaking, the electronic band structure of a photocatalytic semiconductor material can significantly affect the optical absorption properties.⁴³ A red shift of absorption edge is observed for the WS₂@MoS₂ composite in comparison with pristine structures, which verifies that the narrowed band gap of the composite. These results are also in agreement with the electronic properties analyzed above.

In the following part, we will determine the band offsets using the first-principles by the potential-line-up method.^{44, 45} In the potential-line-up method, the valence band offset (VBO) is usually determined by two terms:⁴⁶ $VBO = \Delta\bar{V} + \Delta V$. The first contribution $\Delta\bar{V}$ is referred as the band structure term, which

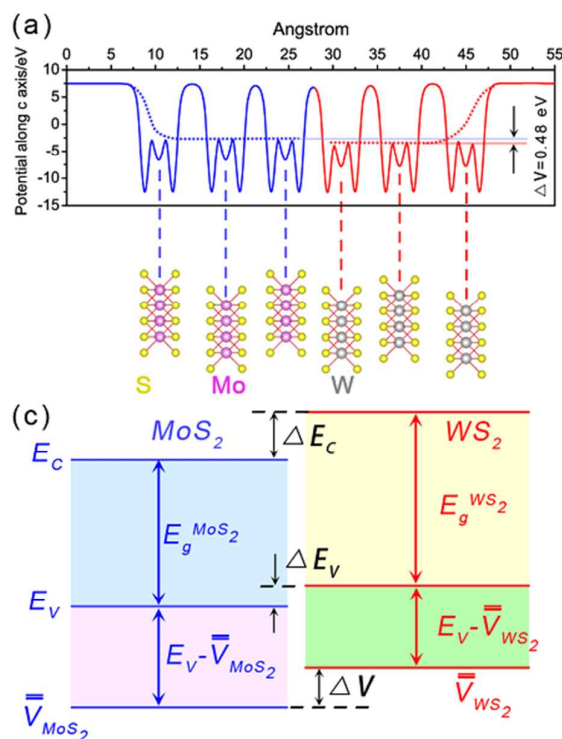


Fig. 8 (a) Macroscopic average potential from WS₂ to MoS₂ in the heterojunction. (b) Band alignment schematic diagram of the WS₂@MoS₂ heterojunction.

is the characteristic of the individual bulks. It is defined as the difference between the top of the valence bands as obtained from two independent standard bulk band-structure calculations at the same strained geometries as in the supercell calculation. The second term ΔV denotes the lineup of the macroscopic average of the self-consistent electrostatic potential across the interface. Because of the well known inherent defect of DFT method to describe excited states, we use the recently reported experimental band gaps of WS₂ and MoS₂ ($E_{gap}^{WS_2} = 1.3eV, E_{gap}^{MoS_2} = 1.2eV$).⁴⁷ Thus, the conduction band offset (CBO) can be evaluated using the simple relation $CBO = \Delta E_V + E_{gap}^{WS_2} - E_{gap}^{MoS_2}$.

The average potential $\bar{V}(z)$ and macroscopic average potential $\bar{V}(z)$ schematic of the WS₂@MoS₂ heterojunction is plotted in Fig. 8a, which shows oscillation patterns of the average potential attributing to the periodicity of the supercell. The macroscopic average potential in the interface shows a discontinuity of $\Delta V = 0.48eV$. According to the above definition, the value of the VBO is $\Delta E_V = 0.14 eV$, and the CBO is calculated as 0.24 eV, implying the formation of the well-defined type-II staggered band alignment.

Generally, a staggered band alignment at the interface will lead to the electrons or/and holes trapped in the spike, incurring the reduced surface photochemical activity. The accurately calculated band alignment of WS₂@MoS₂ using the first-principles method indicates that the WS₂@MoS₂ composite structure shows the well-defined staggered type-II

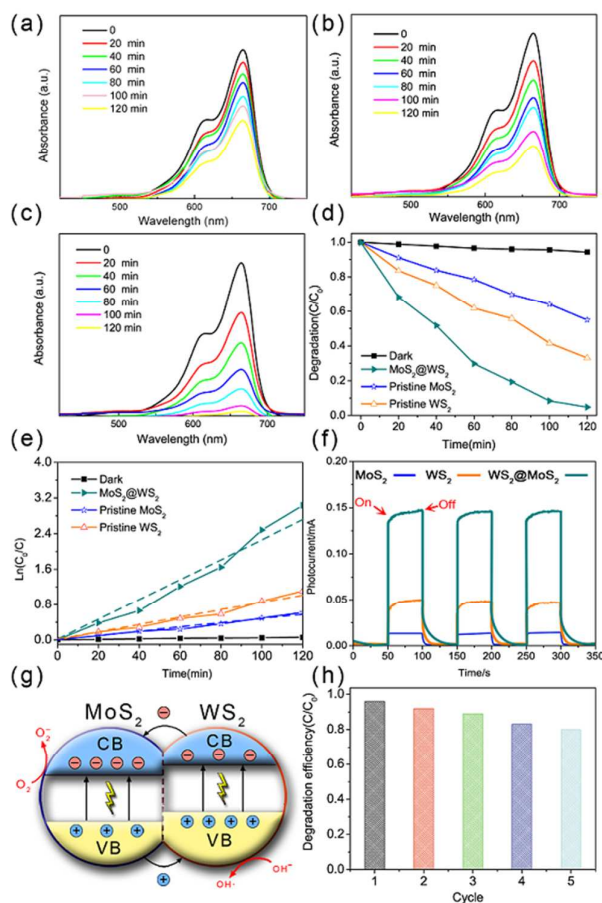


Fig. 9 (a-c) The absorption spectra of MB solution after 120 min irradiation at room temperature in the presence of pristine MoS₂, WS₂ and MoS₂@WS₂ composite, respectively. (d) The normalized C/C₀ concentration decrease for the MB solution containing different catalysts. C and C₀ are the residual and initial concentration of MB, respectively. (e) Logarithm (ln(C₀/C)) of the normalized concentrations vs. irradiation time. Dashed lines denote the data fitting curves of the t against ln(C₀/C). (f) Photocurrent responses of pristine WS₂/MoS₂ and MoS₂@WS₂ electrodes in Na₂SO₄ solutions under visible light irradiation. (g) Schematic diagram of the charge transfer mechanism in MoS₂@WS₂ composite. (h) Repeated photocatalytic degradation of MB solution by MoS₂@WS₂ composite under visible light irradiation.

band alignment and can provide an effective carrier separation in this composite based photoelectric devices. As for the previously reported heterojunction based structures, Yang *et al.*⁴⁸ fabricated the Cu₂O-ZnO heterostructure by magnetron sputtering. The VBO/CBO of 2.91/1.71 eV and 2.52/1.32 eV were obtained for Cu₂O@ZnO and ZnO@Cu₂O, respectively. Huang *et al.*⁴⁹ deposited thin Cu₂O layers on TiO₂ and it exhibited that the VBO and CBO were estimated to be 2.13 and 0.73 eV, respectively. It should be noted that Khanchandani *et al.*⁵⁰ designed ZnO@CdS and ZnO@Ag₂S core-shell nanostructures with the same shell thickness. The MB degradation results indicated that ZnO@Ag₂S core-shell nanostructures exhibited 40- and 2-fold constant enhancement in comparison with pristine ZnO and ZnO@CdS core-shell heterostructure, respectively. They considered that the improved photocatalytic ability was originated from a smaller CBO between ZnO and Ag₂S, which would facilitate the charge separation at the interface. Need of special note is that Hong *et al.*⁵¹ recently reported the first experimental

observation of the ultrafast charge transfer in atomically photoexcited thin MoS₂@WS₂ heterostructures verified by photoluminescence mapping and femtosecond pump-probe spectroscopy measurements. Their experiments showed that the holes would transfer from MoS₂ layer to WS₂ layer within 50 fs after optical excitation, which was a remarkable rate for van der Waals coupled 2D layers. Based on the above analyses, an assertion is furthered that this ultrafast charge transfer characteristic is originated from the relatively small band offset that can greatly promote the transfer of carriers. Anyhow, a further more accurate experiments should be conducted to verify this conclusion in the future. In this work, the calculated band offsets are indeed much smaller in comparison with the above mentioned heterojunctions, implying this WS₂@MoS₂ heterogeneous structure may also be available for the photocatalysis usage.

In the following photocatalysis experiment, MB is used to evaluate the photocatalysis abilities of the synthesized catalysts. Fig. 9a to c show the variation of absorption in the presence of pristine MoS₂, WS₂ and MoS₂@WS₂ composite, respectively. The continually reduced absorption indicates the gradually decreased concentration of MB with increasing of the reaction time. Fig. 9d presents the dependency of the degradation rate within the irradiation time of 120 min. A degradation of MB solution without photocatalyst is also conducted and almost no photocatalytic decolorization of MB solution is observed after irradiation for 120 min as indicated in the black line of Fig. 9d. This explains the stability of MB under long time irradiation. Accordingly, catalyst plays a key role in the process of degradation under irradiation. Before irradiation, the mixed solution of catalysts and MB were stirred in dark to establish the adsorption/desorption equilibrium on the surface of catalysts. After irradiation for 120 min, C/C₀ significantly reduce to 54.9 % and 33.1 % for pristine MoS₂ and WS₂, respectively. A large amount of rim and edge sites of WS₂/MoS₂ are considered as the active sites for the photodegradation of MB,⁵² since the edge sites have strong interaction with the positively charged MB molecules for unstable dangling bonds.

The absorption spectra of WS₂@MoS₂ are shown in Fig. 9c. It is shown that the MB solution containing WS₂@MoS₂ hetero-nanostructure presents a much faster peak-descending tendency than that of pristine MoS₂ and WS₂ nanostructure. According to the above experiments, it is apparent that the photocatalytic activity of the composite structure is much better than that of the pristine catalysts. After 120 min irradiation for WS₂@MoS₂ under the same conditions, the degradation curves prove that the composite possesses the optimal photocatalytic performance than other pristine structures. Besides, the photocatalytic degradation rate of organic pollutants is often expressed by the Langmuir-Hinshelwood (L-H) equation,⁵³ which originated from a simple saturation kinetics mechanism. It can be expressed as $\ln(C_0/C) = kt + A$, where C₀ and C represents the pollutant concentrations in solution at time t₀ and t, respectively, and k denotes the photodegradation rate. The k for various photocatalysts can be obtained by plotting ln(C₀/C) versus t,

and the k values obtained from the slopes of the fitted lines. As shown in Fig. 9e, all data fitting curves of the t against $\ln(C_0/C)$ are nearly linear, the rate constant of pristine MoS_2/WS_2 are 0.005 and 0.009 min^{-1} , respectively, while a much higher rate constant of 0.026 min^{-1} is obtained for the $\text{WS}_2@\text{MoS}_2$ hetero-nanostructure. In order to further investigate the carriers separation abilities of the different catalysts, the photocurrent responses measurements are performed for the three photoelectrodes. As shown in Fig. 9f, all three electrodes under intermittent irradiation in Na_2SO_4 solution demonstrate apparent photocurrent responses. The fast and uniform responses to each light on/off interval of the three photoelectrodes indicate the good reproducibility of the corresponding samples. The pristine WS_2/MoS_2 structures exhibit relatively low photocurrents, implying the low quantum efficiency of WS_2/MoS_2 . In contrast, the composite shows a much elevated photocurrent intensity than that of two pristine structures. It is generally believed the photocurrent is mainly originated from the separation of photogenerated charges within the photoelectrode, in which electrons are transported to the back contact while holes are taken up by the hole acceptors in the electrolyte. A higher photocurrent response of the composite suggests that heterostructure do have a positive effect on the restrain of recombination for photogenerated charges.⁵⁴ Based on the above measurements, the enhanced photodegradation ability of $\text{WS}_2@\text{MoS}_2$ composite can be ascribed to the specific charge-transfer kinetics as shown in Fig. 9g. When the $\text{WS}_2@\text{MoS}_2$ hetero-nanostructure is formed, the built-in electric field facilitates the separation of e^- and h^+ , thus photocatalytic abilities can be improved for the restrained recombination. This conclusion is also firmly supported by the above comprehensive scientific calculations. The photo-excited electrons react with the oxygen in the water to produce radical anions, meanwhile, valence band holes are captured by water molecules to form hydroxyl radicals to photo-oxidize organic molecules eventually. Besides the photocatalytic performances, the stability is also important for the practical application of photocatalyst. So the cycle runs are also conducted to evaluate the stability of the composite under irradiation. All processes and parameters remain the same as the corresponding procedures. As indicated in Fig. 9h, the results showed that the activity of composite was maintained at about 81.2% after 5 cycles compared with the maximum degradation of 95.1% for the first run. It clearly indicates the composite was stable during the photocatalytic degradation process.

4 Conclusion

In conclusion, a simple and efficient 2-step approach had been proposed to fabricate the novel dual-petals nanostructured $\text{WS}_2@\text{MoS}_2$ involving ball-milling, annealing and hydrothermal methods approaches. The mechanical ball-milling was believed to play a crucial role in the formation of the separated WS_2 NPs, leading to a rapid and direct sulfurization of WO_3 . This synthesis approach provided a high-efficiency method for the large-scale fabrication of thin and

separated WS_2 NPs, thus a vast amount of base material was available for the growth of sub-petals of MoS_2 . Due to its unique structural feature with densely attached MoS_2 nanopetals that could provide highly exposed edges as active sites and the formation of type-II stagger energy band, the $\text{WS}_2@\text{MoS}_2$ hybrid catalyst had exhibited high photocatalyst activity. In order to analysis the internal mechanism of this heterogeneous structure comprehensively, we also conducted the electronic and optical properties calculations of the $\text{WS}_2@\text{MoS}_2$ composite by the first-principles method. It was revealed that the band gap of the $\text{WS}_2@\text{MoS}_2$ composite was narrowed compared with those of the pristine WS_2 and MoS_2 . Besides, the $\text{WS}_2@\text{MoS}_2$ composite had a perfect stagger type-II band alignment, thus the photoexcited electron could be injected into the conduction band of MoS_2 from that of WS_2 . The proper interface charge distribution facilitated the carriers separation at the $\text{WS}_2@\text{MoS}_2$ interface region. The carriers separation and electron injection could prevent the recombination of electron-hole pairs. The calculated absorption coefficients indicated an obvious redshift of the absorption edge. In brief, this original work not only successfully fabricated the dual-petals nanostructured $\text{WS}_2@\text{MoS}_2$ that could output the improved photocatalysis activity, but also provided full details based on DFT calculations regarding to the inner mechanisms that facilitated the corresponding performance. It will provide valuable references for the future related studies.

Acknowledgements

The authors acknowledge financial support from the NSF of China (Grant Nos. 61274014, 61474043, 61425004), Innovation Research Project of Shanghai Education Commission (Grant No. 13zz033) and Project of Key Laboratory of Polar Materials and Devices (Grant No. KFKT20140003).

References

- 1 B. Weng, X. Zhang, N. Zhang, Z. R. Tang and Y. J. Xu, *Langmuir*, 2015, **31**, 4314–4322.
- 2 K. Rajeshwar, N. R. de Tacconi and C. R. Chenthamarakshan, *Chem. Mater.*, 2001, **13**, 2765–2782.
- 3 Z. Huang, Z. Chen, Z. Chen, C. Lv, H. Meng and C. Zhang, *ACS Nano*, 2014, **8**, 8121–8129.
- 4 H. Tong, S. X. Ouyang, Y. P. Bi, N. Umezawa, M. Oshikiri and J. H. Ye, *Adv. Mater.*, 2012, **24**, 229–251.
- 5 Y. Wang, X. C. Wang and M. Antonietti, *Angew. Chem., Int. Ed.*, 2012, **51**, 68–89.
- 6 F. Fresno, R. Portela, S. Suárez and J. M. Coronado, *J. Mater. Chem. A*, 2014, **2**, 2863–2884.
- 7 Y. Mao and S. S. Wong, *J. Am. Chem. Soc.*, 2006, **128**, 8217–8226.
- 8 J. Low, S. Cao, J. Yu and S. Wageh, *Chem. Commun.* 2014, **50**, 10768–10777.
- 9 L. Yuan, M. Q. Yang and Y. J. Xu, *Nanoscale*, 2014, **6**, 6335–6345.
- 10 J. X. Xia, Y. P. Ge, D. X. Zhao, J. Di, M. X. Ji, S. Yin, H. M. Li and R. Chen, *CrystEngComm*, 2015, **17**, 3645–3651.

- 11 B. Mahler, V. Hoepfner, K. Liao and G. A. Ozin, *J. Am. Chem. Soc.*, 2014, **136**, 14121–14127.
- 12 M. Chhowalla and G. A. J. Amaratinga, *Nature*, 2000, **407**, 164–167.
- 13 J. Xiao, D. Choi, L. Cosimbescu, P. Koech, J. Liu and J. P. Lemmon, *Chem. Mater.*, 2010, **22**, 4522–4524.
- 14 W. Zhou, Z. Yin, Y. Du, X. Huang, Z. Zeng, Z. Fan, H. Liu, J. Wang and H. Zhang, *Small*, 2013, **9**, 140–147.
- 15 S. Jana, P. Bera, B. Chakraborty, B. C. Mitra and A. Mondal, *Appl. Surf. Sci.*, 2014, **317**, 154–159.
- 16 Z. Z. Wu, B. Z. Fang, A. Bonakdarpour, A. Sun, D. P. Wilkinson and D. Z. Wang, *Appl. Catal. B-Environ.*, 2012, **125**, 59–66.
- 17 M. Viršek, M. Krause, A. Kolitsch, A. Mrzel, I. Iskra, S. D. Škapin and M. Remškar, *J. Phys. Chem. C*, 2010, **114**, 6458–6463.
- 18 H. Farag, K. Sakanishi, M. Kouzu, A. Matsumura, Y. Sugimoto and I. Saito, *Ind. Eng. Chem. Res.*, 2003, **42**, 306–310.
- 19 J. G. Tao, J. W. Chai, X. Lu, L. M. Wong, T. I. Wong, J. S. Pan, Q. H. Xiong, D. Z. Chi and S. J. Wang, *Nanoscale*, 2015, **7**, 2497–2503.
- 20 L. Xiao, X. M. Li, X. B. Zang, M. Zhu, Y. J. He, K. L. Wang, D. Xie and H. W. Zhu, *Nanoscale*, 2015, **7**, 8398–8404.
- 21 G. Compagnini, M. G. Sinatra, G. C. Messina, G. Patanè, S. Scalese and O. Puglisi, *Appl. Surf. Sci.*, 2012, **258**, 5672–5676.
- 22 X. P. Ren, L. Q. Pang, Y. X. Zhang, X. D. Ren, H. B. Fan and S. Z. Liu, *J. Mater. Chem. A*, 2015, **3**, 10693–10697.
- 23 J. W. Seo, Y. W. Jun, S. W. Park, H. Nah, T. Moon, B. Park, J. G. Kim, Y. J. Kim and J. Cheon, *Angew. Chem. Int. Edit.*, 2007, **46**, 8828–8831.
- 24 P. G. Li, M. Lei, X. F. Wang, H. L. Tang and W. H. Tang, *J. Alloy. Compd.*, 2009, **474**, 463–467.
- 25 Z. H. Zhou, Y. L. Lin, P. G. Zhang, E. Ashalley, M. Shafa, H. D. Li, J. Wu and Z. M. Wang, *Mater. Lett.*, 2014, **131**, 122–124.
- 26 Y. H. Tan, K. Yu, J. Z. Li, H. Fu and Z. Q. Zhu, *J. Appl. Phys.*, 2014, **116**, 064305.
- 27 J. Z. Li, K. Yu, Y. H. Tan, H. Fu, Q. F. Zhang, W. T. Cong, C. Q. Song, H. H. Yin and Z. Q. Zhu, *Dalton Trans.*, 2014, **43**, 13136–13144.
- 28 J. H. Zhang, F. Z. Ren, M. S. Deng and Y. X. Wang, *Phys. Chem. Chem. Phys.*, 2015, **17**, 10218–10226.
- 29 N. Feng, W. B. Mi, Y. C. Cheng, Z. B. Guo, U. Schwingenschlögl and H. L. Bai, *ACS Appl. Mater. Interfaces*, 2014, **6**, 4587–4594.
- 30 S. Grimme, *J. Comput. Chem.*, 2006, **27**, 1787–1799.
- 31 Y. Feldman, V. Lyakhovitskaya and R. Tenne, *J. Am. Chem. Soc.*, 1998, **120**, 4176–4183.
- 32 H. B. Yang, S. K. Liu, J. X. Li, M. H. Li, G. Peng and G. T. Zou, *Nanotechnology*, 2006, **17**, 1512–1519.
- 33 H. T. Wang, Z. Y. Lu, D. S. Kong, J. Sun, T. M. Hymel and Y. Cui, *ACS Nano*, 2014, **5**, 4940–4947.
- 34 S. S. Xu, X. M. Gao, M. Hu, J. Y. Sun, D. S. Wang, F. Zhou, L. J. Weng and W. M. Liu, *Surf. Coat. Tech.*, 2014, **238**, 197–206.
- 35 B. Chilukuri, U. Mazur and K. W. Hipps, *Phys. Chem. Chem. Phys.*, 2014, **16**, 14096–14107.
- 36 J. Wang, Z. Guan, J. Huang, Q. Li and J. Yang, *J. Mater. Chem. A*, 2014, **2**, 7960–7966.
- 37 W. Tang, E. Sanville and G. Henkelman, *J. Phys.: Condens. Matter*, 2009, **21**, 084204.
- 38 M. Y. Yin, X. C. Wang, W. B. Mi and B. H. Yang, *Comp. Mater. Sci.*, 2015, **99**, 326–335.
- 39 P. Liang, B. Tai, H. B. Shu, T. Shen and Q. M. Dong, *Solid State Commun.*, 2015, **204**, 67–71.
- 40 L. Xu, W. Q. Huang, L. L. Wang, Z. A. Tian, W. Y. Hu, Y. M. Ma, X. Wang, A. L. Pan and G. F. Huang, *Chem. Mater.* 2015, **27**, 1612–1621.
- 41 S. L. Zhang, Z. Yan, Y. F. Li, Z. F. Chen and H. B. Zeng, *Angew. Chem. Int. Ed.*, 2015, **54**, 3112–3115.
- 42 F. Wu, Y. Liu, G. Yu, D. Shen, Y. Wang and E. Kan, *J. Phys. Chem. Lett.*, 2012, **3**, 3330–3334.
- 43 L. Sun, Y. Qi, C. J. Jia, Z. Jin and W. Fan, *Nanoscale*, 2014, **6**, 2649–2659.
- 44 A. Baldereschi, S. Baroni and R. Resta, *Phys. Rev. Lett.*, 1998, **61**, 734.
- 45 L. Colombo, R. Resta and S. Baroni, *Phys. Rev. B*, 1991, **44**, 5572.
- 46 A. Baldereschi, S. Baroni and R. Resta, *Phys. Rev. Lett.*, 1988, **61**, 734.
- 47 M. Thirupuranthak, R. V. Kashid, C. S. Rout and D. J. Late, *Appl. Phys. Lett.*, 2014, **104**, 081911.
- 48 M. J. Yang, L. P. Zhu, Y. G. Li, L. Cao and Y. M. Guo, *J. Alloys Compd.*, 2013, **578**, 143–147.
- 49 L. Huang, F. Peng and F. S. Ohuchi, *Surf. Sci.*, 2009, **603**, 2825–2834.
- 50 S. Khanchandani, P. K. Srivastava, S. Kumar, S. Ghosh and A. K. Ganguli, *Inorg. Chem.*, 2014, **53**, 8902–8912.
- 51 X. P. Hong, J. Kim, S. F. Shi, Y. Zhang, C. H. Jin, Y. H. Sun, S. Tongay, J. Q. Wu, Y. F. Zhang and F. Wang, *Nat. Nanotechnol.*, 2014, **9**, 682–686.
- 52 M. Daage and R. R. Chianelli, *J. Catal.*, 1994, **149**, 414–427.
- 53 X. H. Wang, J. G. Li, H. Kamiyama, Y. Moriyoshi and T. Ishigaki, *J. Phys. Chem. B*, 2006, **110**, 6804–6809.
- 54 H. Simelys, H. Diana, S. Adriano, C. Angelica, L. Andrea, C. Valentina, T. Elena and S. G. Saracco, *Phys. Chem. Chem. Phys.*, 2015, **17**, 7775–7786.

Graphical Abstract

A prominent enhanced photocatalytic ability of the $\text{WS}_2@\text{MoS}_2$ heterojunction was obtained. The first-principles calculation showed that the well-defined type-II stagger energy band was formed for the composite structure.

